

Landau-Zener-Stückelberg Spectroscopy of a Superconducting Flux Qubit

Shuang Xu and Yang Yu*

National Laboratory of Solid State Microstructures and Department of Physics, Nanjing University, Nanjing 210093, China

Guozhu Sun

Institute of Superconductor Electronics and Department of Electronic
Science and Engineering, Nanjing University, Nanjing 210093, China

Department of Physics and Astronomy, University of Kansas, Lawrence, KS 66045, USA

(Dated: October 17, 2018)

We proposed a new method to measure the energy spectrum of a superconducting flux qubit. Different from the conventional frequency spectroscopy, a short triangle pulse is used to drive the qubit through the anticrossing and generates Landau-Zener-Stückelberg interference patterns, from which the information of the energy spectrum can be extracted. Without installing microwave lines one can simplify the experimental setup and reduce the unwanted effects of noise. Moreover, the method can be applied to other quantum systems, opening the possibility of calibrating and manipulating qubits with linear pulses.

PACS numbers : 85.25.Cp, 03.67.Lx

I. INTRODUCTION

It has been shown, both theoretically and experimentally, that superconducting devices based on Josephson junctions are ideal architectures successfully displaying macroscopic quantum phenomena¹. On Josephson junction devices, typical quantum phenomena like quantum tunneling²⁻⁴, energy level quantization⁵ and coherent superpositions⁶⁻⁹ have been predicted and experimentally demonstrated. Temporal evolution of quantum states and Rabi oscillations have been observed in macroscopic sense^{10,11}. By virtue of the convenience in engineering, many new ideas are expected to be implemented with Josephson junction devices; one of them is quantum computation^{1,12}. The basic requirement of quantum computation is a quantum bit (qubit). In practice, accurate, efficient and stable manipulations on qubits are the prerequisites of quantum computation. People have proved Josephson Junction devices as a promising candidate for a qubit^{1,6,11,13,14}. Furthermore, integrated multi-qubit control has been attempted with Josephson Junction devices¹⁵⁻¹⁹.

In order to control a qubit with high fidelity, first of all, we have to measure the energy spectrum of the qubit. Conventional spectroscopy utilizes frequency resonance to measure the absorption spectrum of the qubit. This method originates from the historical frequency spectroscopy that has been applied to atoms or molecules^{20,21}. In the case of Josephson junction devices, which are often referred as artificial “atoms”, people inject microwaves to the junction circuit and measure the absorption spectrum. However, this method becomes challenging if the energy is over 10 GHz, because microwaves of this high frequency are hard to optimize with common electronic devices. Although high frequency microwave sources are available, they are expensive and the signal becomes noisy after passing multipliers. Transmission lines and waveguides also limit the applications due

to restricted bandwidth²². To overcome this challenge, some groups have developed alternative techniques such as photon-assisted tunneling²³. In 2008, Berns *et al.* proposed a method called amplitude spectroscopy²⁴. They drove a flux qubit with a microwave of 0.16 GHz, whose amplitude was as large as to sweep through anticrossings in higher energy levels and produced Landau-Zener-Stückelberg (LZS) interference. They observed diamond-like interference patterns, from which the information of energy levels with energies up to 100 GHz was extracted. However, microwaves have phase indeterminacy, which introduces decoherence of the qubit and leads to difficulties in exact manipulations. So we propose another method replacing microwaves with a short triangle pulse. We have studied the LZS interference generated by a triangle pulse sweep. With simulations we have obtained the LZS interference patterns, which encode the information of the spectrum. Remarkably, this technique is also useful in coherent manipulations on quantum systems because the signal length can be set within a sufficiently short time.

This article is organized as follows. In Section II we shall introduce the model in our simulations. Section III is devoted to the results and analytical explanations of a two-level system. In Section IV we take a further step to study the case of a multi-level system. Conclusions are made in Section V.

II. MODEL

The qubit under our discussion is similar to the one in the experiment by Berns *et al.*²⁴. It is a superconducting flux qubit built with a superconducting loop interrupted by three junctions. The qubit is biased with an external flux Φ_{ext} around $\Phi_0/2$, where $\Phi_0 \equiv h/2e$ is the flux quantum. The potential of the qubit has the double-well shape parameterized by the flux bias. According to quan-

tum mechanics, there are quantized energy levels located in both wells. If the noises are suppressed to a sufficiently low degree (much smaller than the energy gaps), quantum behaviors can be observed. We label the localized states as $|Ln\rangle$ (left well) and $|Rn\rangle$ (right well), where $n = 0, 1, 2, \dots$, counting from the ground state. In the basis composed of the localized states, the Hamiltonian of the qubit has non-zero off-diagonal elements, which mark the interwell tunneling. Diagonalizing the Hamiltonian and calculating its eigenvalues, we obtain the spectrum of the qubit theoretically. The spectrum is often parameterized by the flux detuning $\Phi_{ext} - \Phi_0/2$, as drawn in Fig.(1). There are anticrossings at certain values of the flux bias, avoiding energy degeneracy of the two states in different wells when they are tilted to the same energy by the external flux bias. In regions other than the vicinities of the anticrossings, the energy varies linearly with the flux bias, which is a valid approximation in common cases.

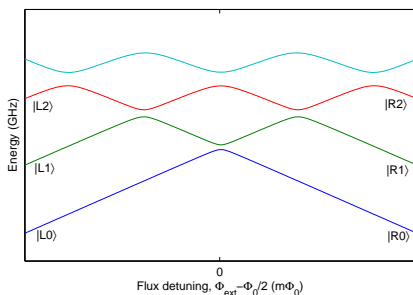


FIG. 1: (color online) Typical energy-level diagram of a flux qubit, showing the relation between the energy and the flux detuning $\Phi_{ext} - \Phi_0/2$.

The study of Landau-Zener transitions and Stückelberg-type interference in a qubit has lasted for a long time^{24–30}. Usually, the experiments are carried out as follows. The qubit is initialized at the ground state in a well, e.g. $|L0\rangle$. Then a microwave signal is injected through the bias line. After some periods of sweeping, the population in a certain state is measured by using a dc SQUID juxtaposed aside the qubit to detect the loop current direction, which is decided by the state of the qubit. The previous works have observed clear interference patterns and managed to extract useful data from the patterns. In our simulation, we follow the same key steps, but have changed some details. First, our sweep signal is a linear triangle pulse, which can be accurately programmed and generated. This seems a minor change but brings great convenience to the experimenters. Moreover, this is closer to the type of transitions originally studied by Zener so Zener’s formula³¹ is of higher accuracy in our work. Second, we measure the system every time when a single pulse ends. This ensures that we will obtain

the direct result of one-turn interference within the decoherence time of the system. The result has not been disturbed or diminished by effects of the environment or defects. Therefore, it is a convenient operation with both accuracy and efficiency.

Now we simulate the revised process of the LZS interference. We drive the qubit with the time-dependent signal

$$\Phi_{ext}(t) = \Phi_0/2 + \Phi_i + \text{Trgl}(\Phi_f, \tau, t), \quad (1)$$

where Φ_i is the initial flux detuning and $\text{Trgl}(\Phi_f, \tau, t)$ is the triangle signal parameterized by Φ_f and τ , which correspond to the final value of the flux sweep and the time width respectively (shown in Fig.(2a)). The explicit expression is

$$\text{Trgl}(\Phi_f, \tau, t) = \begin{cases} kt & (0 < t < \frac{\tau}{2}) \\ k(t - \tau) & (\frac{\tau}{2} < t < \tau) \end{cases}, \quad (2)$$

where k is the sweep rate

$$k = \frac{2(\Phi_f - \Phi_i)}{\tau}. \quad (3)$$

First we consider the two lowest states $|L0\rangle$ and $|R0\rangle$, that is, to treat the qubit as a pure two-level system. The reduced Hamiltonian is

$$\hat{H}_{red} = \hbar \begin{pmatrix} -\Omega(\Phi_{ext}) & \Delta \\ \Delta & +\Omega(\Phi_{ext}) \end{pmatrix}. \quad (4)$$

$\pm\Omega(\Phi_{ext})$ are energy frequencies of the ground states in two wells; Δ is the tunneling frequency between the two states. In following text we set $\hbar = 1$. When we add signal to Φ_{ext} , the Hamiltonian is time-dependent. We use density matrix to calculate the populations in the states. The density matrix of the qubit is

$$\hat{\rho}(t) = \begin{pmatrix} W_{11}(t) & W_{12}(t) \\ W_{21}(t) & W_{22}(t) \end{pmatrix}. \quad (5)$$

W_{11} and W_{22} are populations in $|L0\rangle$ and $|R0\rangle$ respectively, and obey the unity condition $W_{11} + W_{22} = 1$. W_{12} and W_{21} , which are complex conjugate, mark the coherence of the two states. The time-evolution of the density matrix satisfies the celebrated Louville equation

$$i \frac{d\hat{\rho}(t)}{dt} = -i\tilde{\Gamma}\hat{\rho}(t) + [\hat{H}_{red}, \hat{\rho}(t)]. \quad (6)$$

The decaying rate tensor $\tilde{\Gamma}$ will be ignored because the signal width is much shorter than the decaying time.

We initialize the qubit on $|L0\rangle$, which means that the initial condition is

$$\hat{\rho}(0) = \begin{pmatrix} 1 & 0 \\ 0 & 0 \end{pmatrix}. \quad (7)$$

Solve the Louville equation Eq.(6) to obtain the value of $W_{11}(t)$ at $t = \tau$, the population in $|L0\rangle$ when the sweep signal ends. Choosing ranges for the signal parameters Φ_f and τ , and solving the Louville equation for all combinations of signal parameters within their ranges, we obtain a map showing the final W_{11} versus the two parameters.

III. RESULTS AND ANALYSIS

Shown in Fig.(2) are our simulations. In this case, we preset the spectrum with an energy slope of 2 GHz/m Φ_0 and Δ of 2 GHz. For the signal we have $\Phi_i = -5$ m Φ_0 , τ ranging from 0.01 to 4 ns and Φ_f from -2 to 10 m Φ_0 . The final population in the initial state $|L0\rangle$ oscillates along both axes, demonstrating the constructive interference and the destructive interference. The oscillating periods are determined by the energy parameters of the qubit, so we can extract the qubit spectrum from the interference pattern.

It is easy to obtain an analytical solution, which can quantitatively elaborate the result and give specific steps to extract data. Sweeping through the anticrossing incurs Landau-Zener transitions, giving rise to populations in $|R0\rangle$. When sweeping back to the anticrossing, a phase difference of the two states $|L0\rangle$ and $|R0\rangle$ is accumulated:

$$\varphi = \int_0^{\tau^*} (\nu_1(t) - \nu_0(t))dt. \quad (8)$$

$\nu_0(t)$ and $\nu_1(t)$ are given by the eigenvalues of Hamiltonian (4):

$$\nu_{0,1}(t) = \mp \sqrt{\Omega(t)^2 + \Delta^2}. \quad (9)$$

τ^* is the effective width of the signal, equating the interval of the two times of passing the anticrossing (shown in Fig.(2a)):

$$\tau^* = \frac{2\Phi_f}{k} = \frac{\Phi_f \tau}{\Phi_f - \Phi_i}. \quad (10)$$

Notice that $\Omega(t)$ varies linearly with time

$$\Omega(t) = l(\Phi_{ext} - \Phi_0/2) = l(kt - \Phi_0/2) \quad (0 < t < \tau/2), \quad (11)$$

where l is the slope of the spectrum. Substituting it into the integral Eq.(8) and resetting the time parameter, we have

$$\begin{aligned} \varphi &= \int_0^{\tau^*} (\nu_1(t) - \nu_0(t))dt \\ &= 2 \int_0^{\tau^*/2} 2\sqrt{(lkt)^2 + \Delta^2} dt \\ &= lk\tau^* \sqrt{\left(\frac{\Delta}{lk}\right)^2 + \left(\frac{\tau^*}{2}\right)^2} \\ &\quad + 2\frac{\Delta^2}{lk} \ln \left| \frac{lk\tau^*}{2\Delta} + \sqrt{1 + \left(\frac{lk\tau^*}{2\Delta}\right)^2} \right|. \end{aligned} \quad (13)$$

Using Eq.(3) and Eq.(10) to replace k and τ^* with the original signal parameters, we can write the above equation as

$$\begin{aligned} \varphi &= \frac{\Phi_f \tau}{\Phi_f - \Phi_i} \left(\sqrt{\Delta^2 + (l\Phi_f)^2} \right. \\ &\quad \left. + \frac{\Delta^2}{l\Phi_f} \ln \left| \frac{l\Phi_f}{\Delta} + \sqrt{1 + \left(\frac{l\Phi_f}{\Delta}\right)^2} \right| \right). \end{aligned} \quad (14)$$

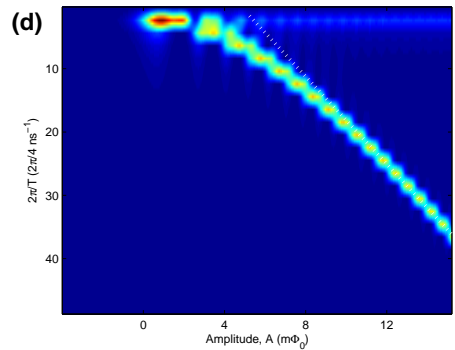
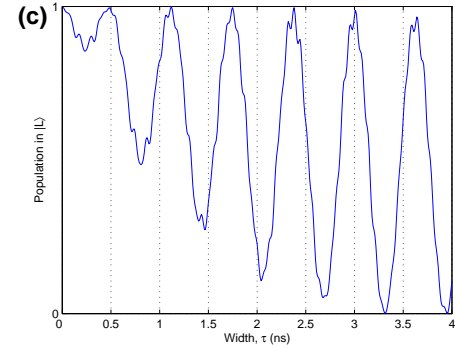
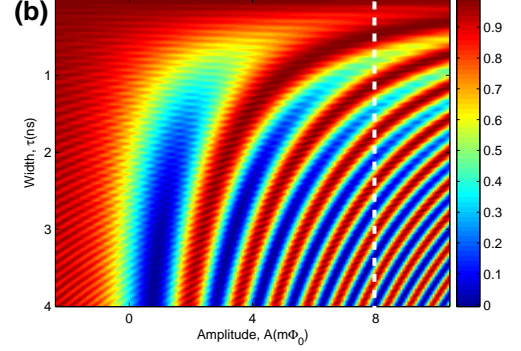
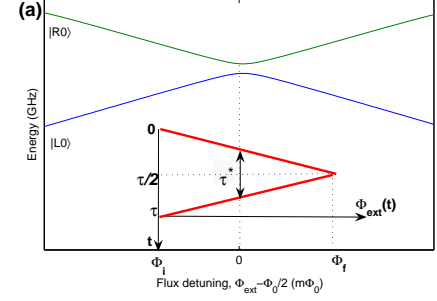


FIG. 2: (color online) (a) Illustration of the qubit spectrum. Only the two lowest levels $|L0\rangle$ and $|R0\rangle$ are taken into account. Preset parameters: the slope is 2 GHz/m Φ_0 and Δ is 2 GHz. The inset shows the details of the signal, with the time width τ and the final value Φ_f . Φ_i is the initial flux detuning and set to be -5 m Φ_0 in this simulation. τ^* is the interval of two times of passing through the anticrossing. (b) The simulation result of LZS interference. The qubit is driven with the signal illustrated in (a). The population in $|L0\rangle$ begins to oscillate when the anticrossing is reached. The data at a large amplitude, e.g. along the white dashed line, can be used to calculate the slope of the energy spectrum. (c) The data on the white dashed line: population in $|L0\rangle$ versus the signal width τ when the amplitude Φ_f is fixed at 8 m Φ_0 . The period of the oscillation is about 0.7 ns. As a fitting parameter,

It is this phase difference that causes the interference. It can be proved that the population in the initial state oscillates sinusoidally with φ ³².

In the limit of large amplitude driving we have

$$\frac{l\Phi_f}{\Delta} \gg 1,$$

thus

$$\varphi \approx \frac{l\Phi_f^2}{\Phi_f - \Phi_i} \tau, \quad (15)$$

from which l can be extracted as the fitting parameter.

To test our method, we extract a section in Fig.(2b) along the white dashed line. This section (see Fig.(2c)) shows the relation between the population in $|L0\rangle$ and the signal width τ at a fixed amplitude that is large enough to validate the approximation in Eq.(15). The oscillation period T is about 0.7 ns. According to Eq.(15),

$$\frac{l\Phi_f^2}{\Phi_f - \Phi_i} = \frac{2\pi}{T} \sim \frac{2\pi}{0.7} \text{ ns}^{-1}.$$

Note that Φ_f is fixed at $8 \text{ m}\Phi_0$ and $\Phi_i = -5 \text{ m}\Phi_0$, the slope is $1.83 \text{ GHz/m}\Phi_0$. Comparing with our preset parameter $l = 2 \text{ GHz}$, we reach a precision of at least 90%. In the extremely amplitude regime, Eq.(15) can be again approximated as

$$\varphi \approx l\Phi_f\tau. \quad (16)$$

Thus,

$$\frac{2\pi}{T} \approx l\Phi_f. \quad (17)$$

To verify this prediction, we extend the calculation range of Φ_f and make a discrete one dimensional Fourier transformation to the interference pattern. The one dimensional Fourier transformation diagram is shown in Fig.(2d). We can clearly observe the linear relation at extremely large values of Φ_f . Actually, when Φ_f is larger than $8 \text{ m}\Phi_0$, the higher levels should be taken into account, as is the case discussed in the following section.

After evaluating l , we can make a further step to extract Δ from Eq.(14). We only need to choose two points in the lower region of Fig.(2b), for instance:

$\Phi_f = 1.0 \text{ m}\Phi_0, \tau = 3.85 \text{ ns}, \text{Population} = 0.00;$

$\Phi_f = 2.0 \text{ m}\Phi_0, \tau = 3.85 \text{ ns}, \text{Population} = 0.93.$

The population on $|L0\rangle$ is equal to³²

$$\frac{1}{2}(1 + \cos \varphi), \quad (18)$$

in which φ can be expressed in terms of Δ as in Eq.(14). So we plot Eq.(18) with Δ as the x -axis and find the value of Δ which fits the both points we have chosen. The result is shown in Fig(3). The only coincident result is $\Delta = 2 \text{ GHz}$, which is also precisely in accordance with our preset parameter.

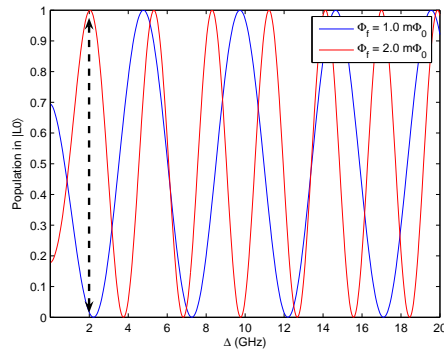


FIG. 3: Plots of the function in Eq.(18) with two sets of parameters. We find that at $\Delta = 2 \text{ GHz}$, both values fit well with the simulation, indicated with the arrow. Thus we obtain the spectrum parameter Δ .

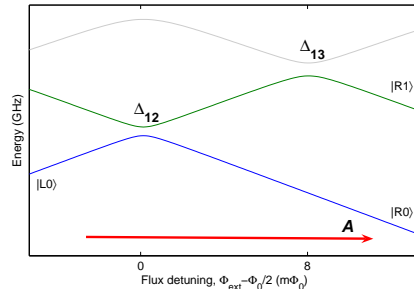


FIG. 4: (color online) Illustration of the spectrum of the three levels in question. Δ_{12} and Δ_{13} mark the sizes of the energy gaps at the anticrossings. The bold arrow illustrates the large amplitudes that sweep through both anticrossings.

IV. MULTI-LEVEL SYSTEM

If we drive the qubit with a signal whose amplitude is large enough to reach another anticrossing in higher energy levels, the interference pattern emerges with interesting characteristics, especially for some sets of parameters. The simulation approach is quite similar to the case in Section III. We consider the three states $|L0\rangle$, $|R0\rangle$ and $|R1\rangle$, as shown in Fig.(4). Under the basis composed of these three states, the reduced Hamiltonian can be written as

$$\hat{H}_{red} = \hbar \begin{pmatrix} \omega_1 & \Delta_{12} & \Delta_{13} \\ \Delta_{12} & \omega_2 & 0 \\ \Delta_{13} & 0 & \omega_3 \end{pmatrix}. \quad (19)$$

Still we will set $\hbar = 1$. ω_1, ω_2 and ω_3 are energy frequencies corresponding to the three states in question. Δ_{12} and Δ_{13} are tunneling frequencies between $|L0\rangle$ and the other two states respectively. They mark the scales of the energy gaps at the two anticrossings. $|R0\rangle$ and $|R1\rangle$ are not correlated.

Now we have a 3×3 density matrix

$$\hat{\rho} = \begin{pmatrix} W_{11} & W_{12} & W_{13} \\ W_{21} & W_{22} & W_{23} \\ W_{31} & W_{32} & W_{33} \end{pmatrix}. \quad (20)$$

The calculation procedures will be the same as in Section III. We have changed the ratio $\Delta_{13} : \Delta_{12}$ and simulated the interference in three cases, each of them having unique characteristics. Now we explain the three cases in details.

Case 1 (Fig.(5a)): $\Delta_{13} = 10$ GHz, $\Delta_{12} = 1$ GHz. We have the ratio $\Delta_{13} : \Delta_{12}$ as large as 10 and obtain an interference pattern that looks similar to the one-anticrossing case. The reason is that the first anticrossing, marked by Δ_{12} , is too small to affect the results. There is no apparent oscillations when $0 < \Phi_f < 8 m\Phi_0$, since strong transitions keep occurring at the vicinities as if there were no energy gaps. So, the interference fringes are caused by the bigger anticrossing, whose location can be easily inferred from the left edge of the first fringe. In this case we find it at $8 m\Phi_0$, in agreement with the spectrum in Fig.(4). Moreover, the parameters related to this anticrossing can also be extracted, following the steps introduced in Section III. However, the information of the smaller anticrossing cannot be obtained because its effects are not revealed in this case.

Case 2 (Fig.(5b)): $\Delta_{13} = 8$ GHz, $\Delta_{12} = 2$ GHz. Then we lower the ratio $\Delta_{13} : \Delta_{12}$ to 4 and then observe a significant difference. The stripes are distorted and irregular when the second anticrossing is reached. The distortion gets slighter as the signal width increases and the pattern becomes close to that in the first case. This can be anticipated because increasing width means slower sweeping and thus gives rise to weaker transitions at the second anticrossing. In the lower part of the map, the pattern resembles that in the one-anticrossing situation, since all that contributes is mainly the first one. Here we can obtain overall information of the energy spectrum, because the two anticrossings are of commensurate sizes that dual effects are observed. We will particularly discuss this case later since it is of special interests.

Case 3 (Fig.(5c)): $\Delta_{13} = 2$ GHz, $\Delta_{12} = 8$ GHz. Now we set the ratio $\Delta_{13} : \Delta_{12} = 1/4$. We encounter a result similar to a one-anticrossing case again. Like the first case, the reason is that the contribution of the smaller anticrossing is rather trivial. It is the first bigger anticrossing that primarily contributes in the small-width region. In the figure we find clear interference fringes from $\Phi_f = 0$, where the first anticrossing is located. And the details concerning this anticrossing can be obtained in the same way as in Section III.

In all the three figures there are very delicate ripples, which result from the high precision of our calculation. While in experiments, the ripples can hardly be observed due to noises, decaying or measurement limits.

Among the three cases we have discussed, the second is of special interests and significance because it is the clos-

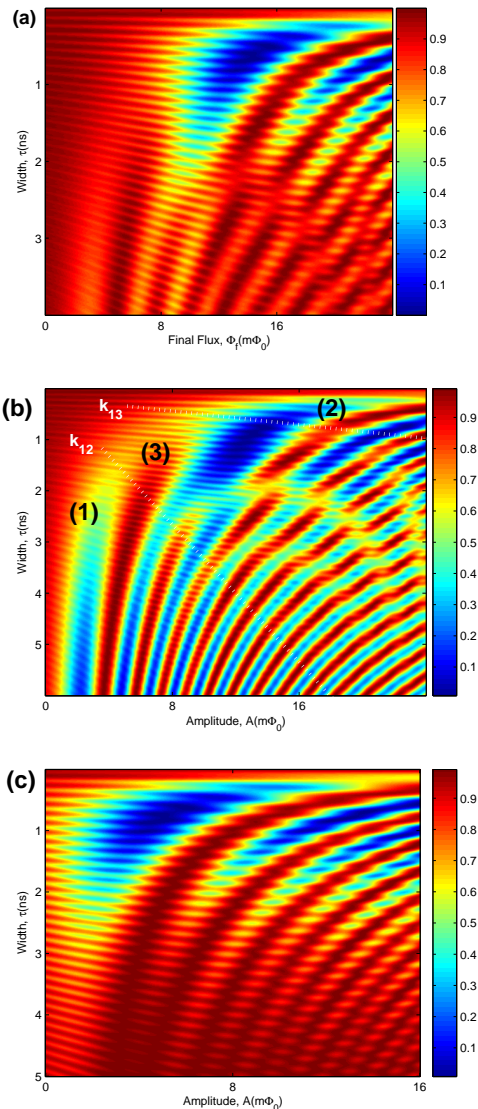


FIG. 5: (color online) Simulation results of LZS interference with two anticrossings involved, marked by Δ_{13} and Δ_{12} respectively. (a) In this case, we have $\Delta_{13} : \Delta_{12} = 10$. The interference fringes primarily result from the bigger anticrossing, which can be located by the left edge of the first fringe. Its parameters can be also obtained by analyzing the pattern as a one-anticrossing case. (b) Commensurate energy gaps are set. The ratio $\Delta_{13} : \Delta_{12}$ is 4. The map can be divided into three regions by two characteristic sweep rates k_{12} and k_{13} , shown with dot lines. In Region(3), distorted interference fringes are observed, due to the cooperative effects of both anticrossings. While in Regions(1) and (2), the pattern is similar to the one-anticrossing case, since one of the anticrossings loses its effect. Thus the information of the anticrossings can be inferred from these two regions respectively. (c) Here $\Delta_{13} : \Delta_{12} = 1 : 4$, resulting in a pattern looking like (a). The big anticrossing overwhelms the small one in most area. Its information can be obtained as well.

est model to the real situation. This is a typical multi-level system with two anticrossings, on which our LZS spectroscopy method is applicable as well. First of all, the locations of the anticrossings can be inferred from the pattern. Similarly, the left edge of the first fringe tells the location of the first anticrossing (at $0 \text{ m}\Phi_0$), and the beginning of the distortion marks the second anticrossing (at $8 \text{ m}\Phi_0$). For further elaborations, we divide the map into three regions with two dashed lines representing two characteristic sweep rates k_{1i} , such that

$$\frac{2\pi\Delta_{1i}^2}{\hbar k_{1i}l} \simeq 1 \quad (\hbar = 1, i = 2, 3),$$

referring to Landau-Zener transition rate formula^{31,33}. In Region(1) where $k \lesssim k_{12}$, the pattern is mainly produced by the first anticrossing Δ_{12} , so we can calculate the energy slope and the value of Δ_{12} . Similarly, in Region(2) where $k \gtrsim k_{13}$, the information of the second anticrossing Δ_{13} can be obtained. Region(3) clearly demonstrates the cooperative effects of both anticrossings and the transition from Region(1), dominated by Δ_{12} , to Region(2), dominated by Δ_{13} . Along the direction of increasing sweep rates, the distortion results in denser stripes. It is because that the bigger anticrossing contributes more when sweeping is faster, so the accumulated phase changes more rapidly, according to Eq.(13).

There have been some experimental results that qualitatively prove our simulations. Recently, some researchers have reported that the spectrum of an rf SQUID is modified by some spurious oscillators. One of the significant works was carried out by Simmonds *et al.* in 2004³⁴. The spurious oscillators, later interpreted as two-level system (TLS), essentially and universally exist in Josephson devices. They transform the energy structure of a phase qubit and lead to multiple anticrossings by coupling with the qubit. One of the latest works on such configuration is held by Sun *et al.*³⁵, who performed Landau-Zener interferometry in a TLS-coupled phase qubit. The spectrum of the qubit shows two TLSs coupled to the system, leading to two anticrossings on the left side of $\Phi_{ext} = \Phi_0/2$. This two-anticrossing structure is similar to the one we have discussed, although their origins are different. Sun *et al.* used triangle pulses to drive the system, and observed the interference fringes characterized by the distortion, which has also been revealed in the second case of our simulations. Notably, Shevchenko *et al.* also have made some deep investigations into this issue very recently³⁶.

Additionally, we want to point out that the method of LZS spectroscopy suggests a possibility of coherent manipulations on a flux qubit. Since the whole process has a time scale of a very short triangle pulse, it ensures that the operation is performed within the decoherence time of the qubit. Moreover, with different sweep rates, we can switch the two anticrossings on and off respectively. The switching sweep rates are exactly the two we have used to divide the map. We can interpret the three regions from an alternative view:

- (1) $k \lesssim k_{12}$. Transitions occur mainly at the first anticrossing but are ignorable at the second, as if the second anticrossing is switched off.
- (2) $k \gtrsim k_{13}$. Now the first anticrossing is switched off while the second is on, because transitions occurring at the first anticrossing are very strong but moderate at the second.
- (3) $k_{12} < k < k_{13}$. This situation corresponds to the region where the two anticrossings are both switched on.

Therefore, the anticrossings act like tunable beam splitters with transmission coefficients changing continuously from null to unit³⁵. By adjusting the sweeping rate carefully, we can control the population in the excited states, supplying an alternative method to manipulate the qubit.

V. CONCLUSIONS

We propose a new method of measuring the energy spectrum of a superconducting flux qubit. By sweeping the qubit through the energy anticrossings with a linear triangle pulse, we obtain the LZS interference patterns. Then by fitting the patterns with analytical equations we can extract the information of the energy spectrum, including the slope of the spectrum and the magnitudes of energy gaps at anticrossings. We have demonstrated this method with numerical simulations. It can be a more convenient and efficient method with a precision over 90%, especially in measuring a spectrum with high energies, in which conventional frequency spectroscopy has difficulties.

Another area where our method may be useful is in the adiabatic quantum computation^{30,37}, in which microwaves are totally unnecessary. If we use this linear spectroscopy to calibrate the qubits, the measurement setup may be simplified and better shielded from the extra noise, which is otherwise introduced from microwave lines.

This method also can be applied to other quantum systems in which rf field coupling may be too weak to generate detectable population transitions, so we can try linear signals instead of rf fields to perform spectroscopy and manipulations.

In addition, since the operation is done within the decoherence time of a qubit, it can be utilized to realize coherent manipulations of the qubit. We have also discussed the approach of controlling the functions of the anticrossings. For our simulations qualitatively agree with related experimental results, we think that our work would stimulate more investigations in this field. Meanwhile, this approach can be extended to multi-qubit systems, whose energy spectra are of analogous structures. Therefore, the approach might also shed light on large-scale controllable quantum computation in future.

Acknowledgments

Thanks to useful discussions with Xueda Wen. This work is partially supported by NSFC (10725415) and

the State Key Program for Basic Research of China (2006CB921801).

-
- * yuyang@nju.edu.cn
- ¹ Y. Makhlin, G. Schön, and A. Shnirman, *Rev. Mod. Phys.* **73**, 357 (2001).
 - ² A. O. Caldeira and A. J. Leggett, *Rev. Mod. Phys.* **46**, 4 (1981).
 - ³ M. H. Devoret, J. M. Martinis, and J. Clarke, *Phys. Rev. Lett.* **55**, 18 (1985).
 - ⁴ S. Han, Y. Yu, X. Chu, S.-I. Chu, and Z. Wang, *Science* **293**, 1457 (2001).
 - ⁵ J. M. Martinis, M. H. Devoret, and J. Clarke, *Phys. Rev. Lett.* **55**, 15 (1985).
 - ⁶ Y. Nakamura, Y. A. Pashkin, and J. S. Tsai, *Nature* **398**, 786 (1999).
 - ⁷ J. R. Friedman, V. Patel, W. Chen, S. K. Tolpygo, and J. E. Lukens, *Nature* **406**, 43 (2000).
 - ⁸ C. H. van der Wal, A. C. J. ter Haar, F. K. Wilhelm, R. N. Schouten, C. J. P. M. Harmans, T. P. Orlando, S. Lloyd, and J. E. Mooij, *Science* **290**, 773 (2000).
 - ⁹ I. Chiorescu, Y. Nakamura, C. J. P. M. Harmans, and J. E. Mooij, *Science* **299**, 1869 (2003).
 - ¹⁰ J. M. Martinis, S. Nam, J. Aumentado, and C. Urbina, *Phys. Rev. Lett.* **89**, 11 (2003).
 - ¹¹ Y. Yu, S. Han, X. Chu, S.-I. Chu, and Z. Wang, *Science* **296**, 889 (2002).
 - ¹² M. A. Nielsen and I. L. Chuang, *Quantum Computation and Quantum Information* (Cambridge University Press, 2000).
 - ¹³ J. E. Mooij, T. P. Orlando, L. Levitov, L. Tian, C. H. van der Wal, and S. Lloyd, *Science* **285**, 1036 (1999).
 - ¹⁴ J. You and F. Nori, *Phys. Today* **58**, 42 (2005).
 - ¹⁵ Y. A. Pashkin, T. Yamamoto, O. Astafiev, Y. Nakamura, D. V. Averin, and J. S. Tsai, *Nature* **421**, 823 (2003).
 - ¹⁶ A. J. Berkley, H. Xu, R. C. Ramos, M. A. Gubrud, F. W. Strauch, P. R. Johnson, J. R. Anderson, A. J. Dragt, C. J. Lobb, and F. C. Wellstood, *Science* **300**, 1548 (2003).
 - ¹⁷ T. Hime, P. A. Reichardt, B. L. T. Plourde, T. L. Robertson, C.-E. Wu, A. V. Ustinov, and J. Clarke, *Science* **314**, 1427 (2006).
 - ¹⁸ L. DiCarlo, J. M. Chow, J. M. Gambetta, L. S. Bishop, B. R. Johnson, D. I. Schuster, J. Majer, A. Blais, L. Frunzio, S. M. Girvin, et al., *Nature* **460**, 240 (2009).
 - ¹⁹ C.-P. Yang, Y.-X. Liu, , and F. Nori, *Phys. Rev. A* **81**, 062323 (2010).
 - ²⁰ A. L. Schawlow, *Rev. Mod. Phys.* **54**, 697 (1982).
 - ²¹ R. C. Thompson, *Rep. Prog. Phys.* **48**, 531 (1985).
 - ²² R. E. Collin, *Foundations for Microwave Engineering* (Wiley-IEEE, 2001).
 - ²³ J. Clarke, A. N. Cleland, M. H. Devoret, D. Esteve, and J. H. Martinis, *Science* **239**, 992 (1988).
 - ²⁴ D. M. Berns, M. S. Rudner, S. O. Valenzuela, K. K. Berggren, W. D. Oliver, L. S. Levitov, and T. P. Orlando, *Nature* **455**, 51 (2008).
 - ²⁵ J. Bylander, M. S. Rudner, A. V. Shytov, S. O. Valenzuela, D. M. Berns, K. K. Berggren, L. S. Levitov, and W. D. Oliver, *Phys. Rev. B* **80**, 220506 (2009).
 - ²⁶ A. V. Shytov, D. A. Ivanov, and M. V. Feigelman, *Eur. Phys. J. B* **36**, 263 (2003).
 - ²⁷ S. Ashhab, J. R. Johansson, A. M. Zagorskin, and F. Nori, *Phys. Rev. A* **75**, 063414 (2007).
 - ²⁸ X. Wen and Y. Yu, *Phys. Rev. B* **79**, 094529 (2009).
 - ²⁹ W. D. Oliver, Y. Yu, J. C. Lee, K. K. Berggren, L. S. Levitov, and T. P. Orlando, *Science* **310**, 1653 (2005).
 - ³⁰ J. Johansson, M. Amin, A. Berkley, P. Bunyk, V. Choi, R. Harris, M. Johnson, T. Lanting, S. Lloyd, and G. Rose, *Phys. Rev. B* **80**, 012507 (2009).
 - ³¹ C. Zener, *Proc. R. Soc. London, Ser. A* **137**, 696 (1932).
 - ³² S. Xu, B.S. Thesis “Landau-Zener-Stückelberg Interference in Josephson Junction Devices” (2010).
 - ³³ L. D. Landau, *Phys. Z. Sowjetunion* **1**, 89 (1932).
 - ³⁴ R. W. Simmonds, K. M. Lang, D. A. Hite, S. Nam, D. P. Pappas, and J. M. Martinis, *Phys. Rev. Lett.* **93**, 7 (2004).
 - ³⁵ G. Sun, X. Wen, B. Mao, J. Chen, Y. Yu, P. Wu, and S. Han, arXiv:1004.4657v2 [cond-mat.supr-con] (2010).
 - ³⁶ S. Shevchenko, S. Ashhab, and F. Nori, *Phys. Rep.* **482**, 1 (2010).
 - ³⁷ E. Farhi, J. Goldstone, S. Gutmann, J. Lapan, A. Lundgren, and D. Preda, *Science* **292**, 472 (2001).